

A15 Phase Ta₃Sb Thin Films: Direct Synthesis and Giant Spin-Orbit Effects

J. S. Jiang^{1,*}, Qianheng Du¹, Ulrich Welp¹, Ramakanta Chapai¹, Hanu Arava¹, Yuzi Liu², Yue Li¹, John Pearson¹, Anand Bhattacharya¹, and Hyowon Park^{1,3}

1. Materials Science Division, Argonne National Laboratory, Lemont, IL 60493

2. Nanoscience and Technology Division, Argonne National Laboratory, Lemont, IL 60493

3. Department of Physics, University of Illinois at Chicago, Chicago, IL 60607

Abstract

We use co-sputtering to directly synthesize thin films of the A15 phase intermetallic compound Ta₃Sb, which has been predicted to have a giant spin Hall conductivity. We identify a large window of Ta:Sb flux ratio that stabilizes single-phase A15 Ta₃Sb. Composition analyses of these films show a Ta:Sb atomic ratio of 4:1, which is consistent with the known Ta-Sb phase diagram. The spin Hall conductivity of thin film Ta₃Sb is $-3400 \pm 400 (\hbar/2e) S/cm$ and the spin-orbit torque efficiency is -0.6 ± 0.1 at 20 K, as determined from harmonic Hall measurements of Ta₃Sb/permalloy bilayer structures. These giant values make Ta₃Sb a promising material for efficient charge-to-spin conversion in spintronic applications. Large field-like spin-orbit effective fields that are independent of the ferromagnetic layer thickness have also been measured in the Ta₃Sb/permalloy bilayers. We attribute the field-like spin-orbit effective field to the Rashba effect at the interface.

Current-induced spin-orbit torques (SOTs) have become a promising tool in spintronic applications to electrically manipulate magnetic moments with a lateral current [1-3]. Of significant interest in implementing SOT-based technologies is the development of materials capable of efficient charge-spin conversion. The efficiency of converting between a charge current j_c and spin current j_s is characterized by the spin-orbit torque efficiency $\xi = (e/\hbar)(j_s/j_c) = (e/\hbar)(\sigma_s/\sigma)$, where σ_s and σ are the spin Hall conductivity and electrical conductivity, respectively. Thus a large σ_s can correspond to a high ξ . Conventional heavy metals such as Pt and β -W have in their electronic structures degenerate bands that are split by spin-orbit coupling (SOC). This leads to non-vanishing Berry curvature which, when integrated over the occupied bands, gives rise to large σ_s [4]. Derunova *et al.* [5] point out that a strategy to search for or design new materials with high σ_s is to maximize Berry curvature by having the Fermi level E_F inside as many small-gapped band crossings as possible. They note that for many intermetallic compounds with the A15 structure, due to their crystalline symmetry (space group 223, $Pm\bar{3}n$), the calculated band structures contain Dirac crossings near E_F if SOC is not considered. These crossings become gapped when SOC is included, leading to giant values of σ_s . It is predicted that the A15 compound Ta₃Sb has a maximum $\sigma_s = -2800 (\hbar/2e) S/cm$ with an eight-fold degenerate Dirac point near E_F . The A15 phase W₃Ta is predicted to have an even larger $\sigma_s = -4500 (\hbar/2e) S/cm$, although only a 9% increase in spin Hall ratio has been reported when β -W is doped with Ta [6]. The modest enhancement was attributed to the less-than-optimal doping level that was achievable.

Because of the large difference in the melting points of Ta and Sb and the high vapor pressure of Sb, direct synthesis of Ta₃Sb has not been possible. Chapai *et al.* [7] synthesized phase-pure powders of A15 Ta₃Sb from the Sb-rich precursor TaSb₂ via a lengthy 14-day thermal decomposition process. The superconducting properties and specific heat of Ta₃Sb were studied

using pellets pressed from the powders. However, due to the porous nature of the powders, it was not possible to fabricate device structures that are necessary to characterize spin-orbit effects.

In this work we directly synthesize thin films of Ta₃Sb from elemental sources using the co-sputtering process. We analyze the structure and charge transport characteristics of the thin films, and identify a large window of processing conditions that can stabilize single-phase A15 Ta₃Sb. The chemical composition of thin film Ta₃Sb deviates from the ideal stoichiometry, but agrees with that of bulk crystals and is consistent with the Ta-Sb phase diagram [8]. From harmonic Hall measurements of Ta₃Sb/Py (Py = permalloy, Ni₈₁Fe₁₉) bilayer structures, giant spin-orbit torque efficiency of -0.6 ± 0.1 and spin Hall conductivity of -3400 ± 400 ($\hbar/2e$) *S/cm* have been measured at 20 K. Large field-like spin-orbit effective fields have also been observed in the Ta₃Sb/Py bilayers and, unlike those in most other spin-orbit heterostructures, they are independent of the Py layer thickness. We attribute the field-like spin-orbit field to the Rashba effect at the interface.

The Ta₃Sb films were grown by magnetron sputtering from elemental Ta and Sb targets. The substrates used were silicon (100) wafers with a native oxide layer. The base pressure of the deposition system before growth was better than 3×10^{-9} Torr. The working pressure of the Ar sputter gas was maintained at 3 mTorr. The source fluxes were set with a calibrated quartz microbalance before deposition, and were measured after deposition to ensure there had been no significant drift. Because of the high vapor pressure of Sb, an over-supply of Sb flux was necessary to compensate for losses during film growth. We varied the substrate temperature and the Ta:Sb flux ratio to search for the optimal growth conditions, guided by crystal structure and phase analyses of XRD measurements.⁹ It was found that, at a substrate temperature of 650°C, a maximum flux ratio of approximately 3:2 was needed for the formation of single-phase A15 Ta₃Sb

films. Further decreasing the flux ratio by up to a factor of 3 did not produce any detectable impurity phase or change in the lattice constant of the A15 structure, suggesting relative stability of the A15 Ta₃Sb in this regime of film growth (see Supplementary Materials for more information). The effective growth rate calculated from deposition times and the film thicknesses measured with X-ray reflectivity (XRR) was approximately 2 nm/min. The Ta₃Sb/Py (Py = permalloy, Ni₈₁Fe₁₉) bilayer structures were prepared by first depositing a 85 nm Ta₃Sb layer and cooling it down in high vacuum to room temperature at a rate of 20°C/min, then Py layers 1 nm- to 10 nm-thick were sputtered at a rate of 6 nm/min. With the exception of the single-layer Ta₃Sb films prepared for composition analyses, all films were capped with 5 nm of MgO before taken out of vacuum. For the electrical measurements, the films were patterned into 6-terminal Hall bar devices using standard optical lithography and argon ion milling. The current channel was nominally 10 μm wide, and 40 μm long between the voltage terminals. The width of the voltage terminals was 5 μm .

Shown in Fig. 1(a) is a representative XRD $2\theta - \omega$ scan of an 85 nm-thick film measured using Cu K_α radiation. The film is polycrystalline. All of the observed diffraction peaks can be indexed to those of Ta₃Sb with the A15 structure. The broad background in the 2θ range of 60°-75° is the residue of the strong Si (200) reflection, which has been mostly removed by an offset in ω of 2.5° from θ . The lattice constant is determined from the peak positions to be $a = 0.5272 \pm 0.0004$ nm, which is very similar to the $a = 0.5274$ nm reported for bulk crystals of Ta₃Sb [7]. Compared with the Ta₃Sb powder diffraction pattern where the (200) peak has less than half the intensity of the (211) peak, the (200) diffraction peak of the sputtered film is nearly twice as strong as the (211) peak, indicating some (200) texturing in the growth direction. From the full width at half maximum of the diffraction peaks we estimate the average coherence length of the Ta₃Sb crystallites to be

about 40 nm in the growth direction. The XRR measurement on an identically-grown Ta₃Sb film is shown in the inset of Fig. 1(a). Fitting the data yields a layer thickness of 84.8 nm and a Ta₃Sb/MgO interfacial roughness of 1.2 nm.

Although the XRD pattern and the lattice constant of the sputtered films match those of the A15 Ta₃Sb, their actual chemical composition deviated from that of the ideal stoichiometry. We analyzed the composition of our films using Rutherford backscattering spectrometry (RBS). As shown in Fig. 1(b), curve-fitting the RBS spectrum taken on a 5.4 nm-thick sputtered Ta₃Sb film yields areal densities of $(43.23 \pm 0.01) \times 10^{15}$ and $(11.04 \pm 0.01) \times 10^{15}$ *atoms/cm²* for Ta and Sb, respectively. This corresponds to a Ta:Sb atomic ratio of 4 : 1, indicating that the film is Sb-deficient. Similar Sb deficiency has been also reported in bulk crystals, and is consistent with the Ta-Sb phase diagram [8], where the A15 phase exists in a narrow homogeneity region that is closer in composition to Ta₄Sb and is characterized by a random mixing of Ta and Sb in the Sb site. As is typically done for A15 compounds, we refer to the sputtered films by their prototypical formula as Ta₃Sb throughout this Letter.

The dark-field (DF) crosssectional TEM image and nanobeam electron diffraction patterns in Fig. 1(c) show the microstructure of an 85 nm Ta₃Sb film. In the DF image, a columnar microstructure is visible where grains are differently-oriented crystalites, as shown by the nanobeam electron diffraction patterns for select areas. The columnar grains are about 10-20 nm wide and only extend to about half the thickness of the film, consistent with the coherence length estimated from the XRD peak widths. Fig. 1(d) displays the HAADF image and the corresponding energy-dispersive X-ray spectroscopy (EDS) maps of Ta and Sb. The EDS maps show uniform distribution of the elements. Since all phases of the Ta-Sb alloy except Ta₃Sb are line compounds,

the lack of modulation in EDS intensity at the length scale of grain sizes confirms that our sputtered film is single-phase.

Figure 2(a) shows the electrical resistivity of thin film Ta₃Sb as a function of temperature between 250 K and 0.7 K. Compared to the bulk powders, the thin film Ta₃Sb is less resistive and has a higher superconducting transition temperature of 0.887K. However, the thin film Ta₃Sb is not metallic, its resistivity has a small negative temperature coefficient of resistivity (TCR), increasing from 177 $\mu\Omega \cdot cm$ at 250 K to 181 $\mu\Omega \cdot cm$ at 2 K. The Hall resistance R_{xy} of a 84.8 nm Ta₃Sb film as a function of the magnetic field was measured at various temperatures and is shown in Fig. 2(b). R_{xy} is linear with fields as high as 14 T, and the slopes are positive, indicating the dominant charge carriers are hole-type. The carrier density decreases slightly with temperature, from $5.4 \times 10^{28} m^{-3}$ at 200 K to $4.8 \times 10^{28} m^{-3}$ at 2 K (see Fig. 2(b) inset). We note that the carrier density is surprisingly high -- comparable to that of typical metals -- despite the negative TCR.

To evaluate the spin Hall conductivity of the Ta₃Sb films, we measured spin-orbit effective fields in in-plane magnetized Ta₃Sb/Py (Py = permalloy, Ni₈₁Fe₁₉) bilayer structures using the harmonic Hall technique [10]. Given that experimental studies of spin-orbit phenomena are prone to spurious effects and that large variations exist in the reported values for properties such as the spin Hall angle, we detail our measurement process and error analyses.

The schematic for harmonic Hall measurements is shown in Fig. 3(a). An ac current with amplitude I_{ac} and frequency $\omega/2\pi = 11$ Hz was applied along the x -axis, and the in-phase first and out-of-phase second harmonics of the longitudinal volage V_{xx} and the transverse voltage V_{xy} were measured simultaneously. Due to the spin-orbit effects in Ta₃Sb and the interface, the ac charge current induces a spin current and spin accumulation, which exert damping-like and field-like spin

torques (or their respective effective fields, H_{DL} and H_{FL}) on the magnetization of Py causing it to oscillate around its equilibrium direction, and give rise to a second harmonic in V_{xy} via the anomalous Hall (AHE) and planar Hall (PHE) effects. At the same time, the Oersted field H_{Oe} from the ac measurement current and thermoelectric effects such as the anomalous Nernst effect (ANE), the spin Seebeck effect (SSE) combined with the inverse spin Hall effect (ISHE), the ordinary Nernst effect (ONE) also contribute to the second harmonic Hall voltage. When the external magnetic field H_{ext} is applied in the xy -plane at an azimuthal angle ϕ with the x -axis, and if the Py magnetization is single-domain with no in-plane anisotropy, the first and second harmonic of the Hall resistance $R_{xy} = V_{xy}/I_{ac}$ are given by [10, 11]:

$$R_{xy}^{\omega} = R_{PHE} \sin 2\phi, \quad (1)$$

$$R_{xy}^{2\omega} = \left[\frac{R_{PHE}(H_{FL}+H_{Oe})}{H_{ext}} \right] \cos \phi \cos 2\phi + \left[-\frac{R_{AHE}H_{DL}}{2(H_{ext}+H_K)} + \frac{\alpha \nabla T}{I_{ac}} + \frac{N \nabla T H_{ext}}{I_{ac}} \right] \cos \phi \quad (2)$$

where R_{PHE} is the saturation planar Hall resistance, R_{AHE} is the saturation anomalous Hall resistance, H_K is the total effective anisotropy field, ∇T is the temperature gradient, α is a coefficient associated with ANE and SSE/ISHE, and N is a coefficient associated with ONE. By exploiting the distinct ϕ - and H_{ext} - dependence of the various contributions, we extracted the values for H_{DL} and H_{FL} from measurements of $R_{xy}^{2\omega}$.

Figures 3(b) and 3(c) show R_{xy}^{ω} and $R_{xy}^{2\omega}$ as functions of ϕ for a Ta₃Sb(84.8nm)/Py(2.0nm) bilayer Hall bar device measured at $I_{ac} = 16$ mA and various in-plane H_{ext} . The measurements were performed at $T = 20$ K to minimize the ϕ -independent offset in the second harmonic signal, and the offsets in both R_{xy}^{ω} and $R_{xy}^{2\omega}$ have been removed. For clarity, only the R_{xy}^{ω} curve for $H_{ext} = 50$ mT is shown in Fig. 3(b), since the Py magnetization is readily saturated by the in-plane field and the amplitude of R_{xy}^{ω} changes by less than 2% between $H_{ext} = 50$ mT and 4 T. The R_{xy}^{ω} curve in

Fig. 3(b) is well fitted with Eq. (1), indicating that the Py magnetization follows the field direction and there is no in-plane magnetic anisotropy. The curve fitting yields $R_{PHE} = 1.76 \text{ m}\Omega$.

The solid lines in Fig. 3(c) are curve fits of the data points to a function with the form $[R_{FL,Oe}] \cos \phi \cos 2\phi + [R_{DL,\nabla T}] \cos \phi$, where $R_{FL,Oe}$ and $R_{DL,\nabla T}$ are fitting parameters. Comparing the fit function to Eq. (1), we have:

$$R_{FL,Oe} = \frac{R_{PHE}(H_{FL}+H_{Oe})}{H_{ext}}, \quad (3)$$

$$R_{DL,\nabla T} = -\frac{R_{AHE}H_{DL}}{2(H_{ext}+H_K)} + \frac{\alpha\nabla T}{I_{ac}} + \frac{N\nabla TH_{ext}}{I_{ac}} \equiv R_{DL} + R_{ANE/SSE} + R_{ONE}. \quad (4)$$

H_{FL} is readily extracted from fitting the H_{ext} -dependence of $R_{FL,Oe}$. Fig. 3(e) displays $R_{FL,Oe}$ as a function of $1/H_{ext}$. The error bars are one standard deviations from the curve fittings. With R_{PHE} already determined, a straight-line fit to the data gives $H_{FL} + H_{Oe} = +0.79 \pm 0.01 \text{ mT}$. From the device channel length and the measured V_{xx} , we estimate the electric field $E = (3.2 \pm 0.2) \times 10^4 \text{ V/m}$, corresponding to a current density in Ta₃Sb of $J_{Ta_3Sb} = E/\rho_{Ta_3Sb} = (1.77 \pm 0.09) \times 10^{10} \text{ A/m}^2$ and a total current in Ta₃Sb of $15 \pm 1 \text{ mA}$. The uncertainties in E and J_{Ta_3Sb} reflect the uncertainties in the device dimensions. The Oersted field is given by Ampere's law, $H_{Oe} = -0.96 \pm 0.05 \text{ mT}$. Therefore, we find $H_{FL} = 1.75 \pm 0.06 \text{ mT}$, and $H_{FL}/J_{Ta_3Sb} = 9.9 \pm 0.5 \text{ mT}$ per 10^{11} A/m^2 .

To extract H_{DL} , we also determined R_{AHE} of the same device by measuring R_{xy}^ω with H_{ext} applied in the z -direction. As shown Fig. 3(d), the positive linear background in R_{xy}^ω at high fields is due to the ordinary Hall resistance of Ta₃Sb, and the anomalous Hall resistance of Py has a simple hard-axis behavior at low perpendicular fields. By extrapolating R_{xy}^ω to $H_{ext}^z = 0$, we obtain $R_{AHE} = 2.03 \text{ m}\Omega$, and the approach to saturation in the anomalous Hall resistance gives the demagnetizing field $H_K = 4\pi M_s = 0.9 \text{ T}$. Fig. 3(f) shows $R_{DL,\nabla T}$ as a function of H_{ext} and its curve

fitting to Eq. (4). Remarkably, $R_{DL,\nabla T}$ has a very significant R_{ONE} component and does not saturate at high fields. As Py is not known to have appreciable ONE, we attribute the large R_{ONE} to Ta₃Sb, because the Nernst effect depends on the density of states (DOS) near the Fermi level and A15 compounds are typically characterized by sharp peaks in their DOS.¹² We note that a large R_{ONE} has also been reported in the topological insulator Bi_{1-x}Sb_x [11]. Since in Fig. 3(e) the linear-in-field R_{ONE} dominates and the curvature in $R_{DL,\nabla T}$ at low H_{ext} is not distinct, we re-plot $R_{DL,\nabla T} - R_{ONE}$ as a function of $1/(H_{ext} + H_K)$ in the inset. The systematic variation of R_{DL} is clearly distinguishable from the scatter of the data that is represented by the error bars, and the curve fit describes the data well. From the fit, we obtain $H_{DL} = -2.6 \pm 0.3 \text{ mT}$, and $H_{DL}/J_{Ta_3Sb} = 15 \pm 2 \text{ mT}$ per 10^{11} A/m^2 . Therefore, the spin-orbit torque efficiency $\xi = (2e/\hbar)\mu_0 M_s t_{Py}(H_{DL}/J_{Ta_3Sb})$ is determined to be -0.6 ± 0.1 and the spin Hall conductivity $\sigma_{SH} = \xi/\rho_{Ta_3Sb}$ is $-3400 \pm 400 (\hbar/2e) \text{ S/cm}$.

The measured σ_{SH} in our sputtered A15 Ta₃Sb thin film has the same sign as and is quite close in value to the theoretical prediction of $-2800 (\hbar/2e) \text{ S/cm}$. However, the agreement needs to be treated with caution, because the theoretical prediction is based on band structure calculations for the stoichiometric A15 Ta₃Sb, while our thin films of A15 Ta₃Sb -- as well as bulk crystals of A15 Ta₃Sb -- are stabilized with the chemical composition of Ta:Sb $\sim 4:1$ (or, Ta_{3.2}Sb_{0.8}, to emphasize the replacement of 20% Sb by Ta due to site-mixing). Assuming site-mixing does not change the band structure of Ta₃Sb, we calculated using density functional theory the change in E_F as the occupancy number N_{occ} is varied [13, 14]. Fig. 4(a) shows N_{occ} as a function of E_F computed for the band structure including the spin-orbit effect. Ta_{3.2}Sb_{0.8} has 0.4 more valence electrons per formula unit than Ta₃Sb, we estimate that the extra electrons would increase the E_F by 0.425 eV and would noticeably reduce the spin Hall conductivity when compared to the result

of Ref. [5]. Moreover, as shown in Fig. 4(b), the raised E_F does not intersect with bands that would give rise to hole orbitals and therefore can not account for the positive Hall coefficient observed in our Ta₃Sb films. A better understanding of the effects of off-stoichiometry and disorder in realistic A15 Ta₃Sb on its electronic structure is desirable and is a subject of further study. Nevertheless, the giant spin-orbit torque efficiency $\xi = -0.6 \pm 0.1$ measured in our sputtered A15 Ta₃Sb thin film is one order of magnitude higher than that of Pt ($\xi = 0.08$), making Ta₃Sb a promising material for efficient charge-to-spin conversion in spintronic applications.

The H_{FL}/J_{Ta_3Sb} that we measure in the Ta₃Sb/Py bilayers is significantly larger than those observed in bilayers containing Pt and W.^{15,16} Moreover, it is independent of the Py layer thickness. Fig. 5 shows the measured H_{FL} values as a function of J_{Ta_3Sb} for a series of Ta₃Sb/Py bilayers with Py layer thickness $t_{Py} = 2, 5, 10$ nm. All the data points fall onto one straight line, indicating that the effective field per unit current H_{FL}/J_{Ta_3Sb} is constant even with a five-fold change in t_{Py} . This is in stark contrast to most reports of the field-like spin-orbit torque in nonmagnetic metal/ferromagnet heterostructures,¹⁷⁻²¹ where H_{FL} decreases with increasing ferromagnetic layer thickness t_F , as $1/t_F$ or faster. While the origins of the field-like torques can be either the Rashba effect or the spin Hall effect, there is consensus that the interfacial nature of the Rashba field or spin current dephasing leads to a t_F -independent field-like torque, and therefore $H_{FL} \propto 1/t_F$. On the other hand, semiclassical modeling [22] based on the Boltzmann equation does produce, for the Rashba effect, a field-like *torque* that increases with increasing t_F and therefore an effective spin-orbit *field* that is independent of or weakly dependent on t_F . Our observation of a constant H_{FL}/J_{Ta_3Sb} in Ta₃Sb/Py bilayers appears consistent that prediction. We note that a t_F -independent H_{FL}/J has also been reported in GeTe/Py bilayers, where GeTe is a ferroelectric Rashba semiconductor with strong Rashba spin-orbit coupling.²³ In the Ta₃Sb/Py bilayers, besides the

inversion symmetry breaking at the interface, the predicted^{5,24} topologically nontrivial surface state along the Ta₃Sb (001) could also be a source of Rashba-like spin-orbit coupling.

In summary, we have synthesized by co-sputtering A15-phase Ta₃Sb thin films that exhibit giant spin Hall conductivity. The wide window of processing conditions allows for facile and direct synthesis of the material. These properties make A15 Ta₃Sb a promising material for efficient charge-spin conversion. The off-stoichiometric nature of A15 Ta₃Sb highlights the need for better understanding its electronic structure. We have observed in the Ta₃Sb/Py bilayer structure large field-like spin-orbit effective fields that are independent of the Py layer thickness, and we attribute them to the Rashba effect at the interface.

ACKNOWLEDGEMENT

We acknowledge Dr. Timothy Spila for the acquisition of RBS data. Work at Argonne National Laboratory was supported by the U.S. Department of Energy, Office of Science, Basic Energy Sciences, Materials Science, and Engineering Division. H. Park acknowledges the computing resources provided on Bebop, a high-performance computing cluster operated by the Laboratory Computing Resource Center at Argonne National Laboratory.

Figure captions:

Fig. 1: (a) XRD pattern of an 85 nm sputtered Ta₃Sb film. Inset: XRR data and fit. The slower modulation in intensity is due to the MgO capping layer. (b) RBS data and fit of a 5.4 nm Ta₃Sb film. (c) Dark-field cross-sectional TEM image of an 85 nm Ta₃Sb film. Nanobeam electron diffraction patterns of selected areas A and B are shown. (d) HAADF image and corresponding EDS maps of Ta and Sb showing the elemental distributions.

Fig. 2: (a) Electrical resistivity of an 85 nm Ta₃Sb film plotted as a function of temperature. (b) Hall resistance measured at various temperatures. Inset: the charge carrier density plotted as a function of temperature.

Fig. 3: (a) Schematic of the harmonic Hall measurement. (b) and (c) field angle-dependence of the first and second harmonic Hall resistance of a Ta₃Sb(85nm)/Py(2nm) device measured at 20K under various fields in the xy-plane. The solid lines are curve fits. (d) The first harmonic Hall resistance of the same device measured with an out-of-plane field. The dashed lines indicate extrapolations used to determine the anomalous Hall resistance and the effective anisotropy field. (e) $1/H_{ext}$ dependence of the fitting parameter $R_{FL,0e}$. The solid line is a fit. (f) H_{ext} dependence of the fitting parameter $R_{DL,VT}$. Inset: $R_{DL,VT} - R_{ONE}$ plotted as a function of $1/(H_{ext} + H_K)$. The solid lines are curve fits.

Fig. 4: (a) The change in E_F plotted as a function of the occupancy number for Ta₃Sb. (b) Calculated band structure of Ta₃Sb with SOC included. The dot-dash line indicates the Fermi level when 20% of Sb is replaced by Ta.

Fig. 5: H_{FL} plotted as a function of J_{Ta_3Sb} for a series of Ta₃Sb/Py bilayers.

References

* Corresponding author: jiang@anl.gov

¹ I.M. Miron, G. Gaudin, S. Auffret, B. Rodmacq, A. Schuhl, S. Pizzini, J. Vogel, and P. Gambardella, “Current-driven spin torque induced by the Rashba effect in a ferromagnetic metal layer,” *Nature Mater* **9**(3), 230–234 (2010).

² L. Liu, O.J. Lee, T.J. Gudmundsen, D.C. Ralph, and R.A. Buhrman, “Current-Induced Switching of Perpendicularly Magnetized Magnetic Layers Using Spin Torque from the Spin Hall Effect,” *Phys. Rev. Lett.* **109**(9), 096602 (2012).

³ Q. Shao, P. Li, L. Liu, H. Yang, S. Fukami, A. Razavi, H. Wu, K. Wang, F. Freimuth, Y. Mokrousov, M.D. Stiles, S. Emori, A. Hoffmann, J. Åkerman, K. Roy, J.-P. Wang, S.-H. Yang, K. Garello, and W. Zhang, “Roadmap of Spin–Orbit Torques,” *IEEE Transactions on Magnetics* **57**(7), 1–39 (2021).

⁴ G.Y. Guo, S. Murakami, T.-W. Chen, and N. Nagaosa, “Intrinsic Spin Hall Effect in Platinum: First-Principles Calculations,” *Phys. Rev. Lett.* **100**(9), 096401 (2008).

⁵ E. Derunova, Y. Sun, C. Felser, S.S.P. Parkin, B. Yan, and M.N. Ali, “Giant intrinsic spin Hall effect in W_3Ta and other A15 superconductors,” *Science Advances* **5**(4), eaav8575 (2019).

⁶ M.Z. Minhas, A.K. Pandeya, B. Grover, A. Fumarola, I. Kostanovskiy, B.K. Hazra, W. Hoppe, G. Woltersdorf, A. Bedoya-Pinto, S.S.P. Parkin, and M.N. Ali, “Doping-induced spin Hall ratio enhancement in A15-phase, Ta-doped β -W thin films,” *J. Phys. Mater.* **3**(4), 044001 (2020).

⁷ R. Chapai, A. Rydh, M.P. Smylie, D.Y. Chung, H. Zheng, A.E. Koshelev, J.E. Pearson, W.-K. Kwok, J.F. Mitchell, and U. Welp, “Superconducting properties of the spin Hall candidate Ta_3Sb with eightfold degeneracy,” *Phys. Rev. B* **105**(18), 184510 (2022).

⁸ F. Failamani, P. Broz, D. Macciò, S. Puchegger, H. Müller, L. Salamakha, H. Michor, A. Grytsiv, A. Saccone, E. Bauer, G. Giester, and P. Rogl, “Constitution of the systems $\{V,Nb,Ta\}$ -Sb and physical properties of di-antimonides $\{V,Nb,Ta\}Sb_2$,” *Intermetallics* **65**, 94–110 (2015).

⁹ See Supplementary Information for XRD characterization of Ta-Sb films grown with various source fluxes.

¹⁰ C.O. Avci, K. Garello, M. Gabureac, A. Ghosh, A. Fuhrer, S.F. Alvarado, and P. Gambardella, “Interplay of spin-orbit torque and thermoelectric effects in ferromagnet/normal-metal bilayers,” *Phys. Rev. B* **90**(22), 224427 (2014).

- ¹¹ N. Roschewsky, E.S. Walker, P. Gowtham, S. Muschinske, F. Hellman, S.R. Bank, and S. Salahuddin, “Spin-orbit torque and Nernst effect in Bi-Sb/Co heterostructures,” *Phys. Rev. B* **99**(19), 195103 (2019).
- ¹² B.M. Klein, L.L. Boyer, D.A. Papaconstantopoulos, and L.F. Mattheiss, “Self-consistent augmented-plane-wave electronic-structure calculations for the A_{15} compounds V_3X and Nb_3X , $X=Al, Ga, Si, Ge,$ and Sn ” *Phys. Rev. B* **18**(12), 6411–6438 (1978)
- ¹³ G. Kresse and J. Furthmuller, “Efficient iterative schemes for ab initio total-energy calculations using a plane-wave basis set” *Phys. Rev. B* **54**, 11169 (1996).
- ¹⁴ G. Kresse and D. Joubert, “From ultrasoft pseudopotentials to the projector augmented-wave method” *Phys. Rev. B* **59**, 1758 (1999).
- ¹⁵ K. Garello, I.M. Miron, C.O. Avci, F. Freimuth, Y. Mokrousov, S. Blügel, S. Auffret, O. Boulle, G. Gaudin, and P. Gambardella, “Symmetry and magnitude of spin–orbit torques in ferromagnetic heterostructures,” *Nature Nanotechnology* **8**(8), 587–593 (2013).
- ¹⁶ C.O. Avci, “Fieldlike and antidamping spin-orbit torques in as-grown and annealed Ta/CoFeB/MgO layers,” *Phys. Rev. B* **89**(21), (2014).
- ¹⁷ X. Fan, H. Celik, J. Wu, C. Ni, K.-J. Lee, V.O. Lorenz, and J.Q. Xiao, “Quantifying interface and bulk contributions to spin–orbit torque in magnetic bilayers,” *Nat Commun* **5**(1), 3042 (2014).
- ¹⁸ T.D. Skinner, M. Wang, A.T. Hindmarch, A.W. Rushforth, A.C. Irvine, D. Heiss, H. Kurebayashi, and A.J. Ferguson, “Spin-orbit torque opposing the Oersted torque in ultrathin Co/Pt bilayers,” *Applied Physics Letters* **104**(6), 062401 (2014).
- ¹⁹ S. Emori, T. Nan, A.M. Belkessam, X. Wang, A.D. Matyushov, C.J. Babroski, Y. Gao, H. Lin, and N.X. Sun, “Interfacial spin-orbit torque without bulk spin-orbit coupling,” *Phys. Rev. B* **93**(18), 180402 (2016).
- ²⁰ Y. Ou, C.-F. Pai, S. Shi, D.C. Ralph, and R.A. Buhrman, “Origin of fieldlike spin-orbit torques in heavy metal/ferromagnet/oxide thin film heterostructures,” *Phys. Rev. B* **94**(14), 140414 (2016).
- ²¹ J. Yu, D. Bang, R. Mishra, R. Ramaswamy, J.H. Oh, H.-J. Park, Y. Jeong, P. Van Thach, D.-K. Lee, G. Go, S.-W. Lee, Y. Wang, S. Shi, X. Qiu, H. Awano, K.-J. Lee, and H. Yang, “Long spin coherence length and bulk-like spin–orbit torque in ferrimagnetic multilayers,” *Nature Mater* **18**(1), 29–34 (2019).
- ²² P.M. Haney, H.-W. Lee, K.-J. Lee, A. Manchon, and M.D. Stiles, “Current induced torques and interfacial spin-orbit coupling: Semiclassical modeling,” *Phys. Rev. B* **87**(17), 174411 (2013).

²³ J. Jeon, S.W. Cho, O. Lee, J. Hong, J.Y. Kwak, S. Han, S. Jung, Y. Kim, H.-W. Ko, S. Lee, K.-J. Lee, and H.C. Koo, “Field-like spin–orbit torque induced by bulk Rashba channels in GeTe/NiFe bilayers,” *NPG Asia Mater* **13**(1), 1–9 (2021).

²⁴ M. Kim, C.-Z. Wang, and K.-M. Ho, “Topological states in A15 superconductors,” *Phys. Rev. B* **99**(22), 224506 (2019).

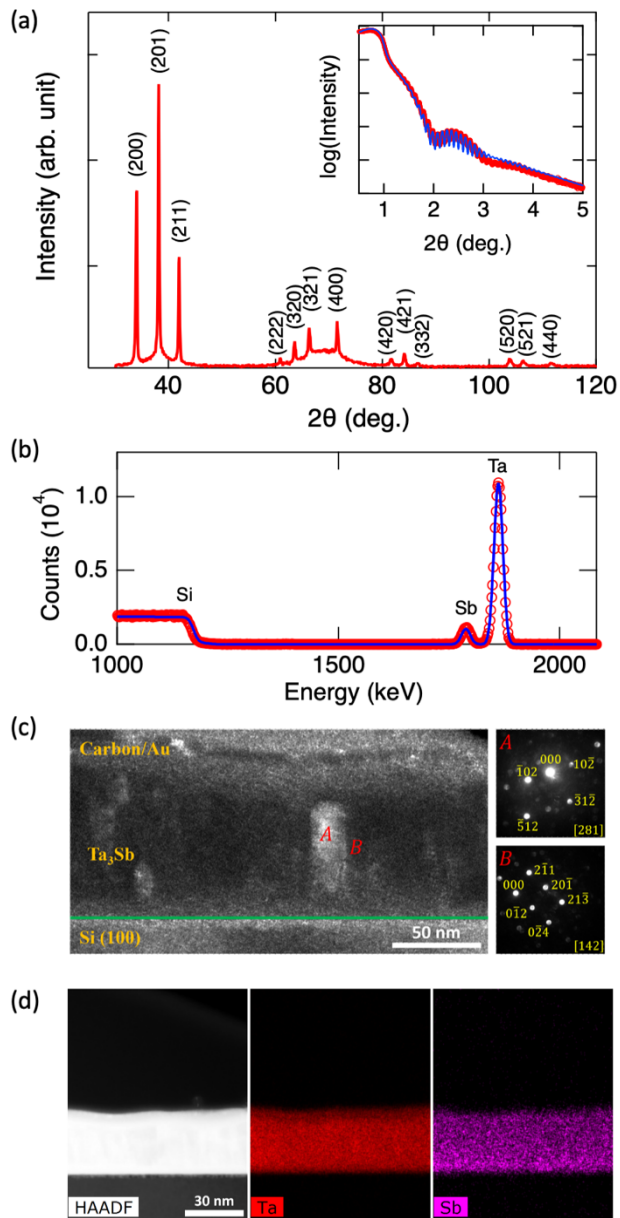


Fig. 1: (a) XRD pattern of an 85 nm sputtered Ta_3Sb film. Inset: XRR data and fit. The slower modulation in intensity is due to the MgO capping layer. (b) RBS data and fit of a 5.4 nm Ta_3Sb film. (c) Dark-field crosssectional TEM image of an 85 nm Ta_3Sb film. Nanobeam electron diffraction patterns of selected areas A and B are shown. (d) HAADF image and corresponding EDS maps of Ta and Sb showing the elemental distributions.

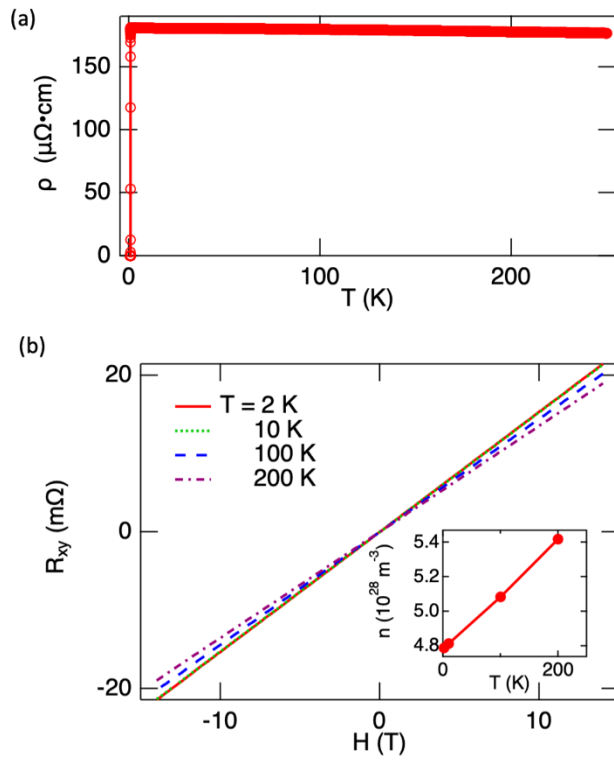


Fig. 2: (a) Electrical resistivity of an 85 nm Ta_3Sb film plotted as a function of temperature. (b) Hall resistance measured at various temperatures. Inset: the charge carrier density plotted as a function of temperature.

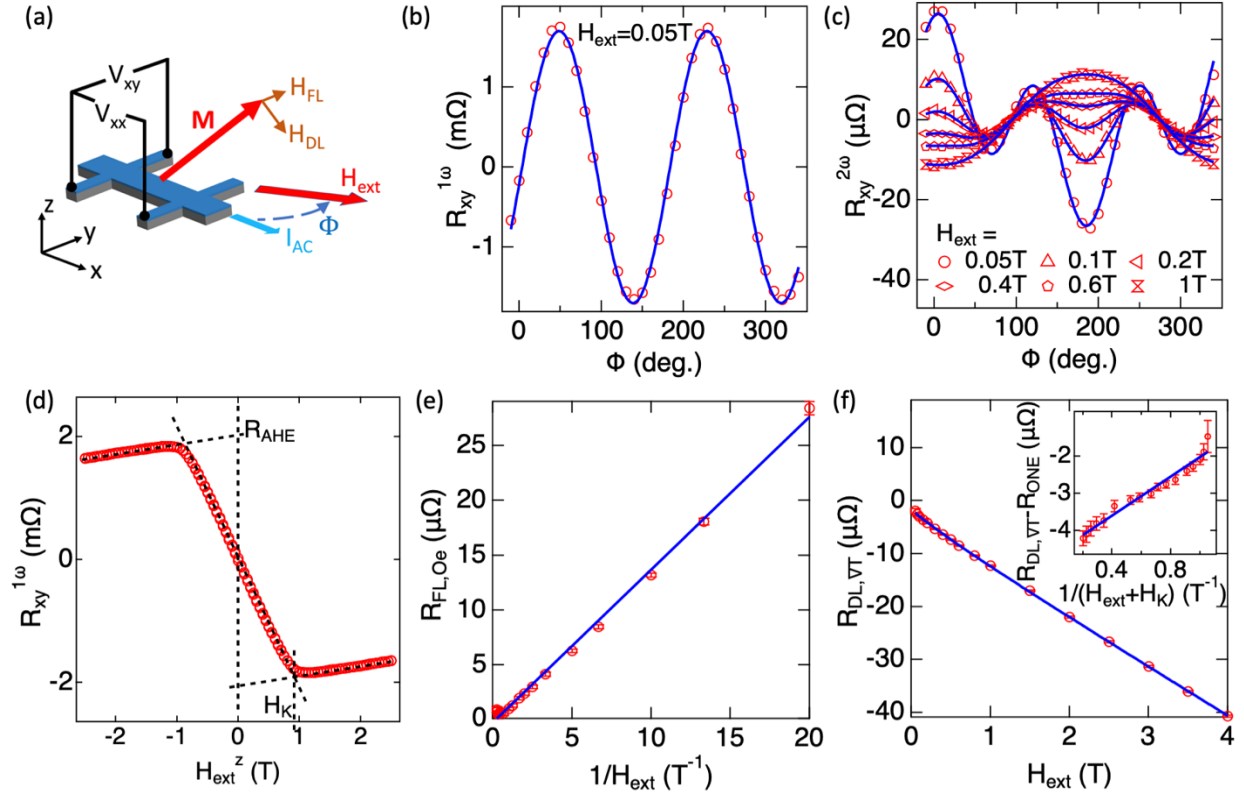


Fig. 3: (a) Schematic of the harmonic Hall measurement. (b) and (c) field angle-dependence of the first and second harmonic Hall resistance of a $\text{Ta}_3\text{Sb}(85\text{nm})/\text{Py}(2\text{nm})$ device measured at 20K under various fields in the xy -plane. The solid lines are curve fits. (d) The first harmonic Hall resistance of the same device measured with an out-of-plane field. The dashed lines indicate extrapolations used to determine the anomalous Hall resistance and the effective anisotropy field. (e) $1/H_{\text{ext}}$ dependence of the fitting parameter $R_{FL,0e}$. The solid line is a fit. (f) H_{ext} dependence of the fitting parameter $R_{DL,VT}$. Inset: $R_{DL,VT} - R_{ONE}$ plotted as a function of $1/(H_{\text{ext}} + H_K)$. The solid lines are curve fits.

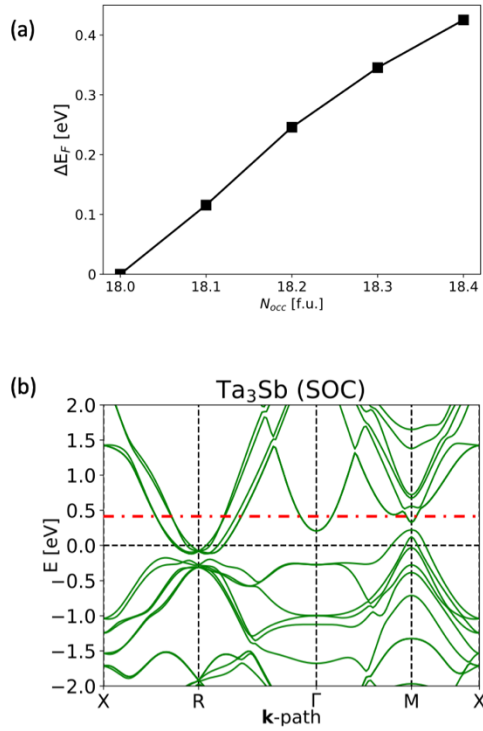


Fig. 4: (a) The change in E_F plotted as a function the occupancy number for Ta_3Sb . (b) Calculated band structure of Ta_3Sb with SOC included. The dot-dash line incate the Fermi level when 20% of Sb is replaced by Ta.

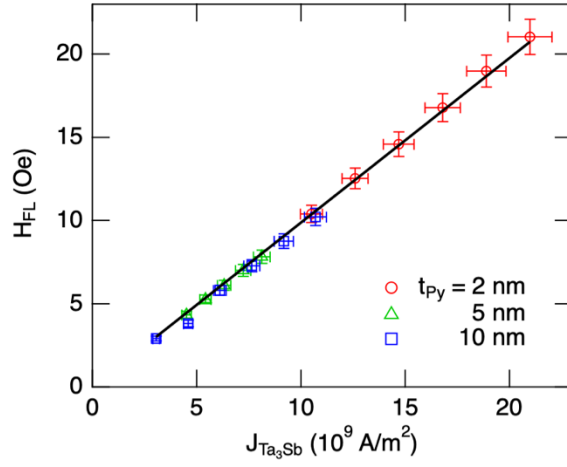


Fig. 5: H_{FL} plotted as a function of J_{Ta_3Sb} for a series of Ta₃Sb/Py bilayers.